Exploring the Impact of Ionic Additives on the Structure and Energetics of Dye-Sensitized NiO Interfaces: Insights from Electrochemistry and First-Principles Calculations

Alekos Segalina, Rita Boaretto, Stefano Caramori, Simone Piccinin, Mariachiara Pastore

Exploring the impact of ionic additives on the structure and energetics of dye-sensitized NiO interfaces: insights from electrochemistry and first-principle calculations

Alekos Segalina,[†,‡,¶] Rita Boaretto,[§] Stefano Caramori,[§] Simone Piccinin,[*,‖] and Mariachiara Pastore[*,¶]

†*Center for Advanced Reaction Dynamics, Institute for Basic Science (IBS), Daejeon 34141, Republic of Korea*

‡*Department of Chemistry and KI for the BioCentury, Korea Advanced Institute of Science and Technology (KAIST), Daejeon, Republic of Korea*

¶*Université de Lorraine & CNRS, LPCT, UMR 7019, F-54000 Nancy, France*

§*Dipartimento di Scienze Chimiche, Farmaceutiche ed Agrarie, Via Fossato di Mortara 17 44121 Ferrara, Italy*

‖*Consiglio Nazionale delle Ricerche, Istituto Officina dei Materiali, CNR-IOM c/o SISSA, Via Bonomea 265, Trieste, Italy*

E-mail: piccinin@iom.cnr.it; mariachiara.pastore@univ-lorraine.fr

Abstract

The efficient functioning of dye-sensitized solar cells (DSSCs) is governed by the interplay of three essential components: the semiconductor, the dye, and electrolyte. While the impact of the electrolyte composition on the device's performance has been extensively studied in n-type DSSCs, much less is known about p-type-based devices. Here we investigate the effect of potential-determining ions on the energetic and stability of dye-sensitized NiO surfaces by using electrochemical , *ab-initio* molecular dynamics (AIMD) simulations, and *ab-initio* electronic structure calculations. The experimental results indicate that the presence of Li^+ leads to a ca. 100 mV positive shift in the potential of NiO, which is in good agreement with what is theoretically predicted (ca. 180 mV). Moreover, both experiments and calculations pinpoint that the presence of Li^+ at the interface weakens the bonds between C343 and NiO, resulting in an accelerated desorption of the dye from the substrate. Computational remodeling of C343@NiO interfaces in the presence and absence of lithium salts (LiF) confirms that the interfacial energetics is very sensitive to the dynamical structure of C343@NiO and to the presence of anionic/cationic species. Indeed, although the presence of lithium at the interface has only a minor impact on the potential difference between NiO and the dye, it significantly influences the electronic coupling between the two interfacial components. This, in turn, leads to variations in the interfacial hole transfer rates.

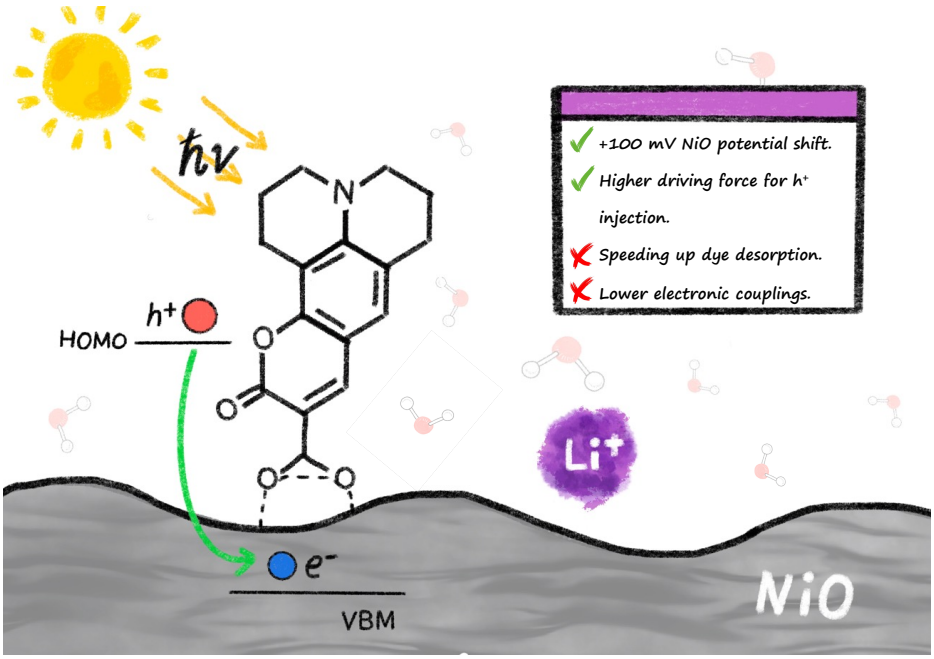
hν
h+
HOMO
N
O
O
O
O
e−
VBM
Li+
NiO
+100 mV NiO potential shift.
Higher driving force for h+ injection.
Speeding up dye desorption.
Lower electronic couplings.

TOC

1 Introduction

Meeting the growing global energy demand while minimizing environmental impact is undoubtedly one of the most pressing societal and technological challenges. Among the renewable energy sources, solar energy offers the great advantages of being both inexhaustible and relatively well distributed across the planet; however, to be harnessed, it must be converted into heat, electricity, or chemical bonds (fuels). In this context, dye-sensitized solar cells (DSSCs)[1–4] and dye-sensitized photoelectrosynthetic cells (DSPECs)[5–8] hold promise for low-cost conversion into electricity and storage of sunlight, respectively. The main components of a DSSC are a wide band-gap metal oxide semiconductor (SC), an organic or metallorganic dye absorbing light in the visible spectrum, and an electrolyte containing a redox couple. Depending on whether the photoactive electrode is embodied by an n-type or a p-type SC, two different devices, with inverse working mechanisms, are configured, namely nDSSCs and pDSSCs, respectively. In nDSSCs (pDSSCs), upon light absorption by the dye an electron (hole) is injected from the LUMO (HOMO) of the photoexcited dye toward the conduction (valence) band of the SC and, in the meantime, an electron (hole) is transferred from the redox shuttle to the dye to regenerate its Ground State (GS) electronic configuration. Finally, the electron (hole) injected into the SC reaches the external load and then the counter electrode where it reduces (oxidizes) the redox shuttle, thus closing the circuit. The same architecture, involving a molecular or supramolecular light absorber grafted onto solid electrodes (n-type and p-type semiconductors for the photoanode and photocathode, respectively) in contact with an electrolyte solution, can also be exploited in a DSPEC. This setup enables the conversion and storage of sunlight into chemical bonds, producing O_2 or a commodity chemical at the anode and fuel at the cathode.

To ensure that in dye-sensitized photoelectrodes the charge transfers successfully occur, the redox potentials, i.e. the energy levels, of the dye, the SC, and the electrolyte or catalysts should be properly aligned. To promote the charge injection process from the dye to the SC, the conduction (valence) band edge of the n(p)-type SC should be lower (higher) in energy with respect to the excited (ground) state potential of the dye. This energy difference, also referred as driving force, is a fundamental parameter that rules the overall performance of the device. As a matter of fact, the maximum efficiency achieved by nDSSCs ($\sim$ 15 %)[9] is about one order of magnitude higher than the one reached by pDSSCs ($\sim$ 2.5 %).[10]

Despite intense research efforts to find valuable alternative p-type SCs,[11–13] the highest-performing photocathodes[14–16] still rely on NiO. This is due to its good electrical conductivity,[17,18] its ability to accept holes from photo-excited dyes in the femtoseconds (fs) timescale,[19–22] and its low cost and easy manipulation. However, NiO also has certain drawbacks, including the presence of intragap trap states and a relatively low interfacial charge transfer resistance. These characteristics promote undesirable charge recombination processes at the NiO/dye/electrolyte interface[17,22] These recombination reactions, which are highly dependent on the film preparation method employed, are related to the high density of defects that generally plague the NiO lattice. To overcome these drawbacks, several attempts of modifying NiO properties through doping, addition of metal cations, and defect passivation/elimination have been reported.[17,23–27]
In particular, the adsorption of small metal cations at the NiO surface remarkably influences the performance

of NiO-based devices, similarly to what has been reported for TiO_2-based DSSCs.[28–33] The presence of adsorbed cations on the NiO surface alters the charge equilibrium at the NiO/dye/electrolyte interface and induces a downshift in the VB edge of the SC,[17,28,29] which has been shown to be proportional to the valence state of the cation.[28] Although the VB edge downshift in principle induces a decrease of the driving force for hole injection, low-valence small metal cations such as Li^+ and Mg^{2+} have been shown to bring a beneficial effect on the efficiency of NiO-based devices.[17,28,29] Similar to Li doping, lithium-based electrolytes, which result in Li adsorption on the NiO surface, enhance charge transfer resistance at the NiO/I_3^-/I^- interface, reducing recombination losses and improving DSSC efficiency. These cations stabilize the electrostatic environment, optimizing conditions that support charge flow and minimize charge recombination. As a result, charge separation is enhanced, leading to improved overall device performance. However, a more recent study suggests that the presence of the electrolyte at the interface may counteract these benefits by stabilizing the hole in the surface trap states of NiO, potentially promoting interfacial charge recombination and contributing to the overall poor performance of pDSSCs.[17,34]

To date, however, a detailed description of the role of the electrolyte composition on the structure and energetics of the dye-sensitized NiO interface is still lacking. Addressing this gap is crucial to provide guidelines for improving NiO-based photoelectrodes. As demonstrated over the past decades, especially for TiO_2[35–38] and perovskite-based[39–41] photovoltaic devices, modern first-principles computational methodologies have proven capable of accurately describing most of the key characteristics of individual systems and their active interfaces, successfully supporting experimental research in the process of device optimization.[3,31,42,43] On the other hand, as far as NiO-dye sensitized interfaces are concerned, only a few computational studies have been reported so far[44–49] and most of them are limited to static DFT calculations in gas phase.[44,47–49] However, as we have shown in our previous works, in order to accurately capture the interfacial energetic alignment between the dye and NiO electronic levels, explicit solvation models, by sufficiently long ab initio molecular dynamic simulations, and highly-expensive GW calculations are required.[45,46] This clearly poses significant challenges for computational investigations, due to the complexity of both the structural model required to simulate the solvated NiO-dye sensitized interface and the advanced methodologies needed to accurately extract its opto-electronic properties.

Here, advancing beyond the state-of-the-art in the simulation of dye-sensitized NiO surfaces, we take a significant step forward in both the complexity of the interface model, by introducing a lithium salts, and the methodology, by extracting electronic coupling elements for the hole transfer and calculating the associated transfer rates for the first time. We studied the solvated coumarin C343-sensitized NiO interface, building on our previous work, and supported our calculations with electrochemical measurements to validate our results. While the C343@NiO system may not be the most efficient p-type sensitized photoelectrode reported so far, its relatively small number of atoms presents the distinct advantage of allowing for extensive ab initio molecular dynamics simulations and accurate electronic structure calculations.[45,46] Moreover, the large availability experimental data for this system enables meaningful comparisons with a wide range of existing studies, facilitating accurate and insightful analyses.[50] By elucidating the behavior of this system and advancing in the simulation of realistic dye-sensitized NiO interfaces, we aim to provide a fundamental understanding of

the functioning mechanisms and the complex interplay between the different interfacial components (solvent, dye, surface, cations), thereby contributing to the enhancement of NiO-based photoelectrode performance.

2 METHODS

2.1 Experimental details

2.1.1 NiO preparation

NiO paste was obtained by ball-milling (2 h) commercially available NiO nanoparticles (In-framat Advanced Materials 20nm) with ethanol (8 mL), glacial acetic acid (0.2 mL), terpineol (3 g), and ethyl cellulose (0.5 g).[51] All reagents and solvents were purchased from Sigma Aldrich and used as received.

2.1.2 Deposition of NiO thin films

NiO thin films were deposited onto a well cleaned fluorine-doped tin oxide (FTO) glass substrates (7 Ω/sq, 2.3mm thick NSG). Cleaning of the conductive glass was performed by sequential immersion and sonication in Alconox and 2-Propanol solutions for 10', followed by 20 min annealing at 450°C in air. The NiO paste was drop cast onto the FTO glass substrates and uniformly spread by spin coating (10 s at 1000 rpm then 20 s at 2000 rpm), followed by drying and thermal sintering in air according to the following temperature program: 25–120 °C (15 min), 120 °C (0 min), 120–450 °C (22 min), 450 °C (30 min), 450–550 °C (10 min), and 550 °C (20 min). The active area of the NiO sample was 1 cm^2.

2.1.3 Sensitization of NiO

Sensitized electrodes were obtained by overnight soaking the NiO films in 0.5 mM Coumarin C343 (Acros organics) in absolute ethanol (Aldrich) at room temperature.

2.1.4 NiO Characterization

NiO film thickness was measured using an Alpha Step D-500 Profilometer (KLA instruments, Milipitas, CA, USA). Data were obtained in step-up/down mode with a scan length of 2 mm at a speed of 0.07 $mm \cdot s^{-1}$ and a stylus force of 5.0 mg. The average thickness of the NiO film was 600 ± 100 nm. The redox properties of NiO and NiO@C343 electrodes were studied by cyclic voltammetry in a conventional three-electrode cell: NiO/FTO was the working electrode, a Pt wire was the counter electrode, and SCE was used as reference. The applied potentials here reported are all given relative to the SCE electrode potential (E vs NHE= 0.241V). The electrolyte was 0.1M LiCl, TBACl (TBA: Tetrabutylammonium) or Li_2CO_3 0.05 M (all from Aldrich) in ultrapure water (Milli-Q water was obtained using a Millipore -Burlington, MA, USA-apparatus, equipped with 0.22 μm filters). Cyclic voltammetry was determined with the potentiostat PGSTAT 302N and recorded with the GPES software. Diffuse reflectance absorption spectra of NiO and NiO@C343 were

recorded with a JASCO V570 spectrophotometer equipped with an integrating sphere (band pass of 5mm). The cyclic voltammetry of C343, performed on NiO at its isoelectric point and as a function of pH, is comprehensively detailed in Section S1 (Figures S1-S4) of the Supporting Information.

2.2 Models and computational details

We carried out *ab initio* molecular dynamics (AIMD) simulations in explicit water and Li^+/F^- ions, for both the dye/semiconductor and bare semiconductor slab. The electronic structure, the hole injection driving force, and the dye/NiO electronic coupling were then calculated for a significant number of snapshots extracted from the AIMD trajectories. In our simulations, we employed Periodic Boundary Conditions (PBC) in all directions. Full details on the calculations are reported below.

2.2.1 Definition of the structural models

To study the effect of the lithium salts on the overall structural properties of the interface, we constructed simulation boxes both in the absence and in the presence of the Li^+/F^- ions. In both cases, the simulation boxes (8.35 × 8.35 × 33.40 $Å^3$) are composed of a NiO@C343 interface consisting of a 6 layers 2×2 slab of NiO, the coumarin dye adsorbed in a bidentate fashion on one of the two NiO(100) surfaces, and by 43 water molecules.[46] It's noteworthy that although our interface model exhibits a high dye concentration (∼1 molecule/0.70 nm^2), it mirrors the typical experimental surface coverage observed in DSSCs.[42]

To model the mere NiO interface in water, we removed the dye from the previous simulation box and filled the space with 9 water molecules, to recover the bulk water density.

In bulk water, the first solvation shell of Li^+ consists of 4 water molecules arranged around the cation into a well defined tetrahedral like shape. Similarly to what happens in TiO_2,[31,52] small cations, such as Li^+, have shown a tendency to adsorb to the surface of NiO.[28] To address this point, we performed AIMD simulations using the thermodynamic integration (Blue Moon Ensemble) approach[53,54] (see Section S7 in the Supporting Information). Our results indicate that Li^+ binds strongly to the NiO surface, with a free energy minimum observed at a distance of 2.1 Å from the surface. Moving Li^+ from this minimum to bulk water has a free energy cost of approximately 1.3 ± 0.1 eV, highlighting the significant electrostatic interaction between the NiO surface and the cation. Thus, when modeling the NiO@C343 interface in the presence of LiF, to accommodate Li^+ close to the surface while retaining its shell of four oxygen atoms, we initially placed the cation in the proximity of one oxygen of the NiO slab and one oxygen of the carboxylic group, as well as two solvent water molecules. Note that varying the Li^+ adsorption site across NiO's surface, including each O^{2-} atoms (7 total), delivered only a marginal impact on electronic properties, as well as on the interfacial energy alignment in our calculations (see Section S4 in the Supporting Information).

The first solvation shell of F^- consists of 6 water molecules, forming an octahedron surrounding the anion. In this work, we consider two model cases: the situation in which the F^- anion remains solvated in the region above the dye, hereafter termed NiO@[Li^+C343]F^-, and when it percolates through the dye monolayer, hereafter termed NiO@[Li^+C343F^-]. For the latter case, three water molecules only have been

initially inserted around the anion. Figure 1 displays the simulated systems, namely the NiO@C343 interface in pure water and the two NiO@C343 interfaces in the presence of Li^+/F^- ions built as illustrated above. Then, to build the NiO solvated interface in the presence of LiF we started from the NiO@[Li^+C343F^-] system, we removed the dye and filled the space with 9 water molecules.

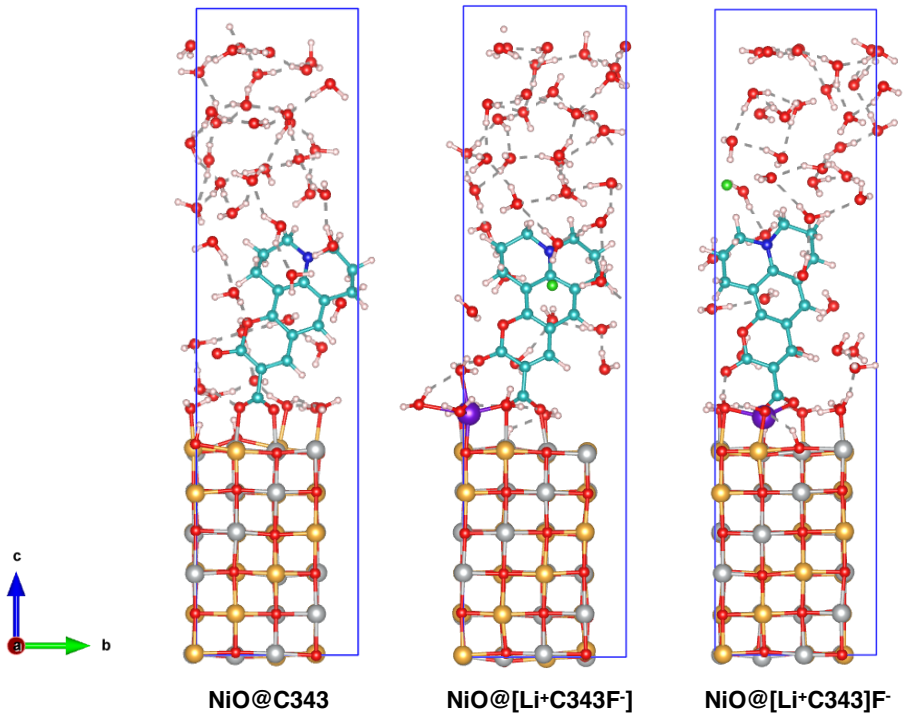

Figure 1: Representative snapshots extracted from the early stages of the MD trajectories of the NiO@C343 interface. The system displayed in the left panel show the interface in pure water solution (**NiO@C343**); the other two systems contain Li^+ (purple) and F^- (green) ions and differ for the anion position; middle panel: F^- located within the C343 monolayer (**NiO@[Li^+C343F^-]**), right panel: the F^- ion located outside the C343 monolayer (**NiO@[Li^+C343]F^-**). Ni atoms polarized up are shown in gold, and Ni atoms polarized down are shown in silver.

2.2.2 AIMD simulations

The AIMD simulations were performed with the CP2K code,[55] adopting the same computational setup already used in our previous works on this system.[45,46] We employed GTH norm-conserving pseudopotentials, the MOLOPT-DZVP-SR basis set, 500 Ry cutoff for charge density, and we sampled the Brillouin zone at Gamma point. We used the PBE exchange and correlation functional, adding a Hubbard term U=2 eV on Ni(d) states. To account for van der Waals interactions, we applied Grimme's D3 correction, including for the substrate only the upmost layer in contact with the water solution. We employed the type-II antiferromagnetic phase (AFII) of NiO, since this is the most stable phase at room temperature and standard pressure. For all the interface systems considered we carried out AIMD simulations in the NVT ensemble, setting the temperature to 360 K via the canonical sampling velocity rescaling thermostat.[56] For NiO@C343 and solvated NiO slab interfaces the AIMD simulations were carried out for 43 ps and 23 ps, respectively,

and in all cases, the first 3 ps were discarded in the subsequent analyses since they are deemed to be the thermalization and equilibration steps. The time step was set to 1 fs throughout the dynamics and we imposed the deuterium mass for hydrogen atoms.

For completeness, before starting the actual AIMD simulations, we optimized the initial configuration for all considered systems, including solvent molecules and any present electrolyte species, for several hundred steps. Although full convergence was not achieved, this process minimized detrimental hydrogen contacts, ensuring a stable and realistic initial structure for the AIMD runs.

2.2.3 Single point DFT calculations

To analyze the electronic structure of the simulated systems and to compute the level alignment across the NiO@C343 interface, we extracted 150 snapshots from the AIMD trajectories and performed single-point DFT calculations. All these calculations were carried out with the Vienna *ab initio* simulation package (VASP),[57–59] projector augmented wave (PAW) pseudopotentials and a plane-wave basis set with a cutoff of 650 eV. Similarly to the AIMD simulations, we sampled the Brillouin zone at the Γ-point, used the PBE functional, and added a Hubbard U term on Ni(d) states adopting Dudarev's approach. For the U-J difference, we used the value of 4.6 eV, self-consistently optimized for NiO..[60] To obtain the valence and conduction bands of bulk NiO, we performed a calculation on the rock-salt structure in the AFII phase, using the experimental lattice constant (4.17 Å) and relaxing the atomic positions. In this case, we used a $8 \times 8 \times 8$ grid of k-points centered at Gamma to sample the Brillouin zone. For the bulk NiO system we also performed G_0W_0 and partially self-consistent calculations GW ($evGW_0$) calculations using the same set up discussed in our previous work.[46] These calculations on bulk structure were preparatory for determining the ionization potential (IP) and electron affinity (EA), as detailed in Section S6 in the Supporting Information.

On the snapshots extracted along MD trajectories, we computed the driving force for the hole injection from the dye to the NiO, defined as the energy difference between the eigenvalue associated with the dye's HOMO and that associated with the NiO's valence band maximum (VBM). To pinpoint the VBM, we computed the projected density of states (PDOS) with a Gaussian broadening of 0.2 eV, focusing solely on the atoms within the NiO slab. Subsequently, we linearly fitted the PDOS corresponding to the highest occupied band of NiO within the window spanning 20% to 80% of the peak height. A visual depiction of this methodology is presented in Figure S11 in the Supporting Information. Details regarding the determination of the dye's HOMO value are provided later in section 2.2.4.

To estimate the electrostatic effect of the Li^+/F^- ions on the absolute position of the HOMO of the dye and of the VB of NiO, we computed the electrostatic potential (V_{el}) along the *c*-axis, perpendicular to the metal-oxide surface (Figure 1), performing a planar average on the *ab*-plane. We then performed a time average using all the snapshots (150) extracted from the AIMD trajectory, and we aligned both the NiO and the dye potential to the bulk water potential. To reduce the oscillations of the V_{el} we computed the macroscopic average using two distinct periods. To flatten the V_{el} in the NiO slab region we used a period of 2.08 Å , corresponding to the average distance between the NiO layers, whereas for the bulk water

potential, we used a period of 2.71 Å, which corresponds to the position of the first peak of the O-O radial pair distribution function of water. To compute the potential in the region of the dye, and therefore to exclude the Li^+/F^- ions and the solvent from the planar average, we constructed spheres centered on the dye's atoms, and considered only points within the spheres for the planar average of V_{el}. We found that a radius of 1.45 Å, was enough to ensure that spheres overlap and, at the same time, to exclude atoms that do not belong to the dye. For the calculation of V_{el} corresponding to the dye, we excluded the atoms belonging to the C343 anchoring group (see the left panel in Figure S12 in Supporting Information), as the localization of the HOMO on the COO^- moiety is negligible. A graphic representation of the points chosen for one specific snapshot is reported in the right panel of Figure S12 in Supporting Information, where one can easily recognize the dye's shape from the points of the V_{el} grid used for the average.

2.2.4 Electronic coupling and hole injection rates calculations

Here we implement a computational protocol to calculate the charge transfer rates at dye-functionalised solid interfaces. This is achieved by estimating the electronic coupling strength between the discrete electronic states of the molecule, the HOMO in this case, and the band states of the semiconductor employing the Newns-Anderson model. To evaluate the electronic coupling between the dye and the substrate, we first calculate the projection of the orbitals of the fully solvated interface, C343@NiO, on the isolated C343 molecule. It is important to note that, to untie the electronic coupling between C343 and NiO to the one coming from the interaction between the dye and the rest of the environmental molecules, one should incorporate the effect of the solvent and, if present, LiF on the dye's wavefunction. In particular, as far as C343 is concerned, we found that the solvent molecules have a strong polarization effect on the Kohn-Sham (KS) orbitals. To take into account this effect, we considered the dye embedded into an implicit solvent utilizing VASPSOL[61] and we set the solvent dielectric constant to 80. To compute the above-mentioned projections, we followed the approach reported in Ref.[62] and briefly summarized below. First, using the LOBSTER code[63] we recast the Kohn-Sham wavefunctions adopting an orthonormal local basis set. Although the local basis set we adopted is orthonormal, the new wavefunctions are no longer orthonormalized because the number of planewaves that describe the PAW bands ordinarily exceeds the number of local basis functions. To restore the orthonormality of the projected wavefunctions, a subsequent Löwdin's symmetric orthonormalization procedure is then applied. The new localized bands can be used to compute the Molecular Orbital Projected Density of States (MO-PDOS), defined as:

$$MO-PDOS_{n_B}(E) = \sum_{n_A,k} w_k |\langle \psi^B_{n_B,k} | \, | \psi^A_{n_A,k} \, | | \rangle|^2 \, \delta(E - \epsilon^A_{n_A,k}) \tag{1}$$

where A and B refer to the C343@NiO interface and the isolated dye, respectively, while w_k weights the k-points sampled in the Brillouin zone. Since in our calculations we resort to Gamma-point approximation, the right-hand side of eq. 1 reduces to the summation of the scalar products and the Dirac delta function. These projections can be used to evaluate the energy of the dye's band of interest, the HOMO in this work,

according to the following equation:

$$E_{HOMO}^{C343@NiO} = \frac{\sum_i p_i \epsilon_i^{KS}}{\sum_i p_i} \tag{2}$$

where the p_i corresponds to the i-th scalar product of eq. 1 evaluated for n_b = HOMO and ϵ_i^{KS} the eigenvalue of the full interface. After determining the HOMO energy using Equation 2, this value is then employed in the computation of the final driving force, as previously outlined.

When the dye is adsorbed on the surface, depending on the extent of the hybridization of its energy levels with those of the semiconductor, *i.e. the electronic coupling*, the HOMO level may undergo an energy shift with respect to the level of the standalone dye, resulting in a lifetime broadening, $\hbar\Gamma$, which is well represented through a Lorentzian shape and can be evaluated using the following formula:[64,65]

$$\hbar\Gamma = \frac{\sum_i p_i |\epsilon_i^{KS} - E_{HOMO}^{C343@NiO}|}{\sum_i p_i} \tag{3}$$

The lifetime broadening computed using Equation 3 represents a direct measure of the extent of electronic coupling between the dye (C343) and the substrate (NiO) and is inversely proportional to the hole-transfer time (τ) through the following relation:[64,65]

$$\tau(fs) = \frac{658}{\Gamma(meV)} \tag{4}$$

3 Results and discussion

3.1 Electrochemistry of NiO and NiO@C343

The cyclic voltammograms of nanostructured NiO (0.5-0.7 μm) films in an aqueous electrolyte solution containing either 0.1 M Li^+ or TBA^+ (tetrabutylammonium) cations show two broad quasi-reversible waves (Figure 2) in agreement with previous observations carried out in other buffered aqueous electrolytes.[66,67] The first more cathodic wave (wave I) is generally attributed to the Ni (II)/(III) process in NiO (Eqs R1 and R2); the second less resolved and generally less intense redox wave, which follows at more positive potential values, could be interpreted as the Ni(II)/Ni(III) oxidation at the surface of the metal oxide followed by the further oxidation of Ni(III) to Ni(IV) (Eqs R1 and R2).[66]

$$NiO\,(OH)_n\,(H_2O)_p \longrightarrow NiO\,(OH)_{n+1}\,(H_2O)_{p-1} + e^- + H^+ \tag{R1}$$

$$NiO\,(OH)_m \longrightarrow NiOO\,(OH)_{m-1} + e^- + H^+ \tag{R2}$$

$$NiO\,(OH)_{n+1}\,(H_2O)_{p-1} \longrightarrow NiO\,(OH)_{n+2}\,(H_2O)_{p-2} + e^- + H^+ \quad \text{(R1)}$$

$$NiOO\,(OH)_{m-1} \longrightarrow NiOO\,(OH)_{m-2} + e^- + H^+ \quad \text{(R2)}$$

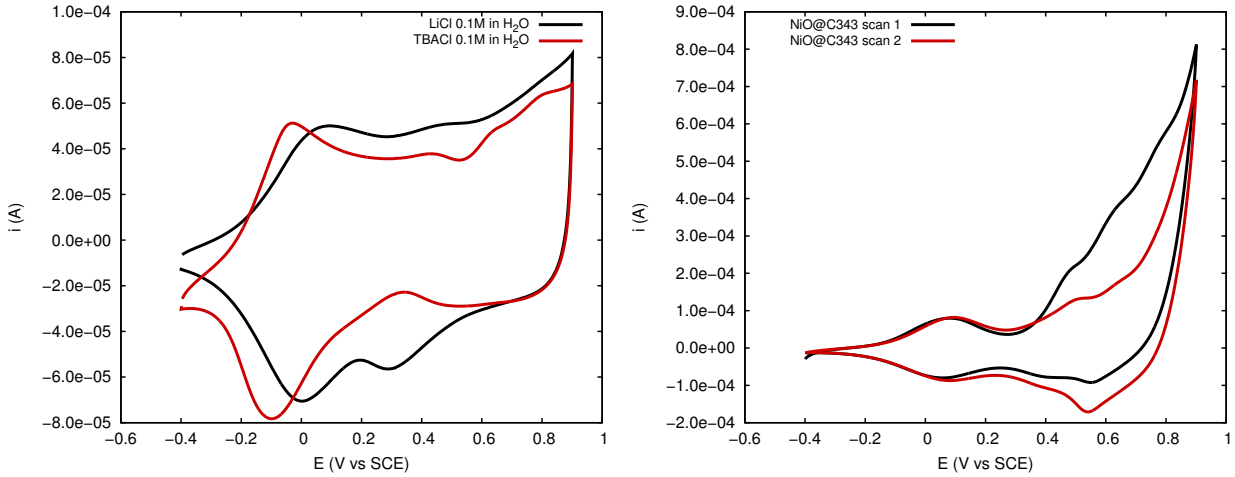

Figure 2: Left panel: Cyclic voltammograms of NiO obtained in two distinct aqueous electrolyte solutions: 0.1M LiCl (black line), and 0.1M TBACl (red line). Right panel: Cyclic voltammograms of NiO@C343 (black line for scan 1; red line for scan 2) obtained in electrolyte solutions: 0.5M Li_2CO_3 in H_2O at pH 10.5 (isoelectric point of NiO). Both the cyclic voltammograms were realized by adopting a scan rate of 20 mVs^{-1}.

Pourbaix diagrams of Ni show that both of these processes are expected to occur within the 0.4-0.5 V vs SCE interval, and are both dependent on the extent of hydration of the metal oxide at the interface with the electrolyte. This explains the lower intensity of the second wave compared to the first one. The composition of the electrolyte affects the energetics of the redox processes in NiO: when Li^+ is present instead of TBA^+, a $\approx$ 100 mV positive shift of wave I is observed. High charge density cations like Li^+ appear to adsorb more strongly at the NiO surface than do TBA^+ ions and are thus potential determining ions for NiO. This is consistent with what has been observed in an aprotic electrolyte (ACN), where no protons are adsorbed to exposed oxygens of NiO.[67] In an aqueous solution, NiO was indeed characterized by a Nernstian behavior, with a slope of ca. 60 mV/pH for the Ni(II)/(III) process of wave I. Wave II was also controlled by pH but the slope of the $E_{1/2}$ (II) vs pH curve (ca. 53 mV/pH) was further from ideality, partly due to a more uncertain $E_{1/2}$ determination due to wave broadening at certain pHs (Figure S1-S2).

NiO films were then sensitized overnight with a 0.5 mM ethanolic solution of C343[68] and the electrochemical properties were studied in water at a pH of 10.5, which is close to the isoelectric point. This was obtained with a solution of 0.05 M Li_2CO_3 adjusted under pHmetric control with dilute HCl. Under these conditions, the sensitized film displays the first Ni(II)/(III) process at 0.07V which is almost identical to the $E_{1/2}$ obtained for pristine NiO (0.08V) (Figure S3). A sequence of at least three irreversible oxidation processes follows the first quasi-reversible wave of the NiO and these are assigned to the irreversible oxidation

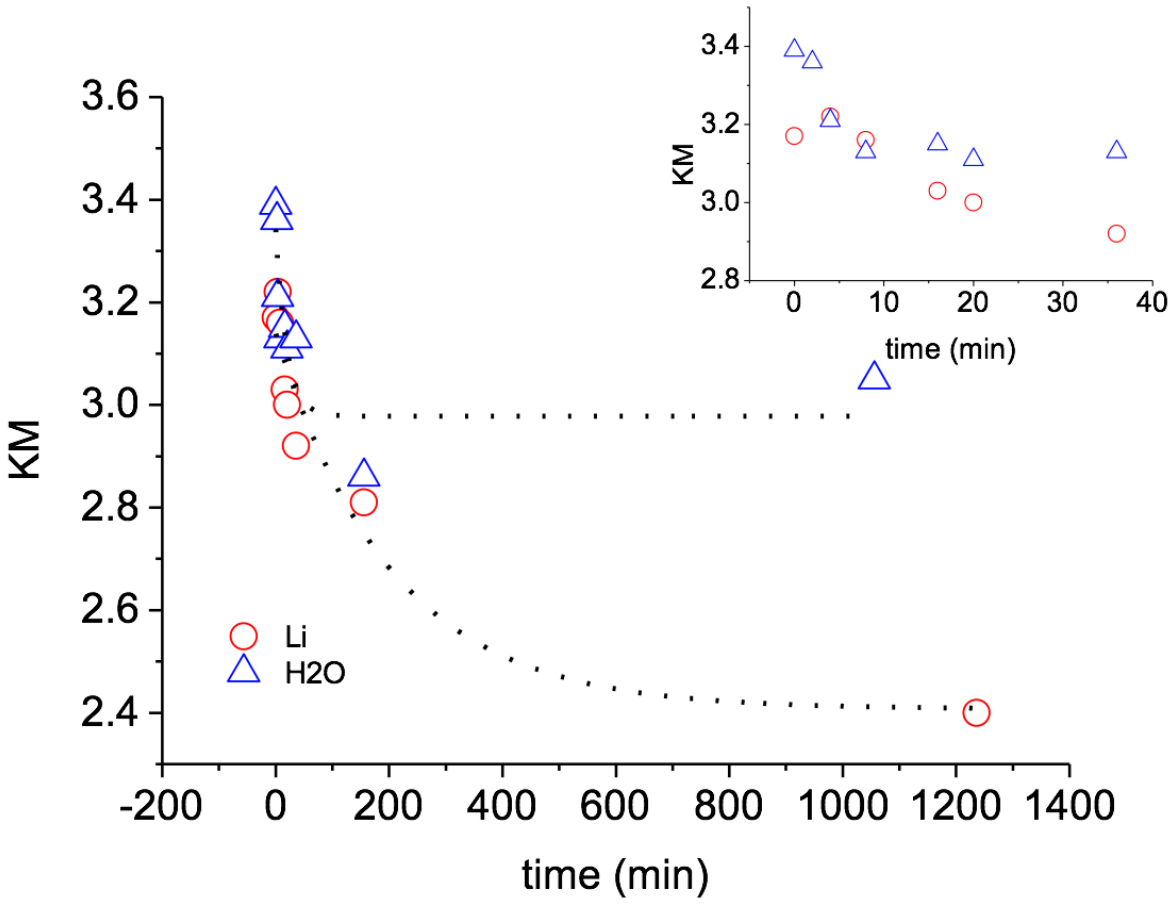

Figure 3: 420 nm absorption, measured in millimolar concentration units (KM), of NiO@C343 recorded during desorption experiments with Li^+ (red circle), or no cations (blue triangle) in H_2O.

of C343 molecules adsorbed to NiO, consistent with the voltammetry of C343 at a glassy carbon electrode reported in Figure S4, where a sequence of three irreversible waves in the 0.5-0.85 V vs SCE interval (Figure S4) was observed. The first wave associated to C343 oxidation practically overlaps with wave II of NiO. The irreversible redox chemistry of C343 results in the irreversible consumption of such coumarin from the NiO surface already during the first voltammetric scan. Indeed, the second scan of the sensitized film bears a close resemblance with that of bare NiO.

Finally, we observed that the interaction of Li^+ with the C343@NiO system weakens the bond between C343 and NiO and promotes rapid desorption when compared with the lithium-free solution. This behavior is highlighted in Figure 3, where the comparative desorption experiments in pure water and in the presence of Li^+ depict faster and larger C343 dye loss from the NiO in the presence of the cation.

3.2 Theoretical band alignment at NiO/water interface

By determining the band alignment at the NiO slab/water interface we can compare our calculated IPs with the experimental oxidation potentials discussed in section 3.1. Details of the band alignment methodology are extensively provided in Section S6 of the Supporting Information.

Figure 4 shows the time average of the macroscopic averaged electrostatic potential computed along the AIMD simulations of the two NiO/water interface systems (with or without LiF). To define a potential inside the semiconductor we consider its value at the center of the slab, while for bulk water we average V_{el} in a 4 Å window centered in the middle of the water region. As can be seen from Table A in the Supporting Information, this is a quite reliable choice, as the bulk water potential shows only minimal changes while varying the thickness of the water slab used for the average.

Table 1: Experimental and calculated IPs (eV) of NiO with and without the Li^+ cation adsorbed at the NiO surface. Theoretical IPs have been computed at different level of theory: PBE+U, G_0W_0@PBE+U, and evGW@PBE+U.

Method	IP(eV)	
	H_2O	Li^+
PBE+U	4.54	4.72
G_0W_0@PBE+U	4.77	4.95
evGW@PBE+U	4.70	4.87
EXP.	4.61	4.72

The calculated NiO's IPs with respect to the vacuum are reported in Table 1. As is apparent, the agreement between the calculated and the experimental data is remarkable. For the NiO slab in pure water the calculated IP, amounting to 4.54 eV, is only 0.06 eV lower than the measured oxidation potential. When LiF is added in the simulation, a downshift of 0.18 eV in the VBM is predicted, in almost quantitative agreement with the experimental value (0.11 eV), and in line with what observed in n-type semiconductors.[30,31,69] It is worth stressing that the small differences we found may be related to a different lithium coverage of the NiO surface or discrepancies between the experimental pH and the one of the model interface, which corresponds to the point of zero charges (PZC). On overall, this result confirms the reliability our computational setup and structural model.

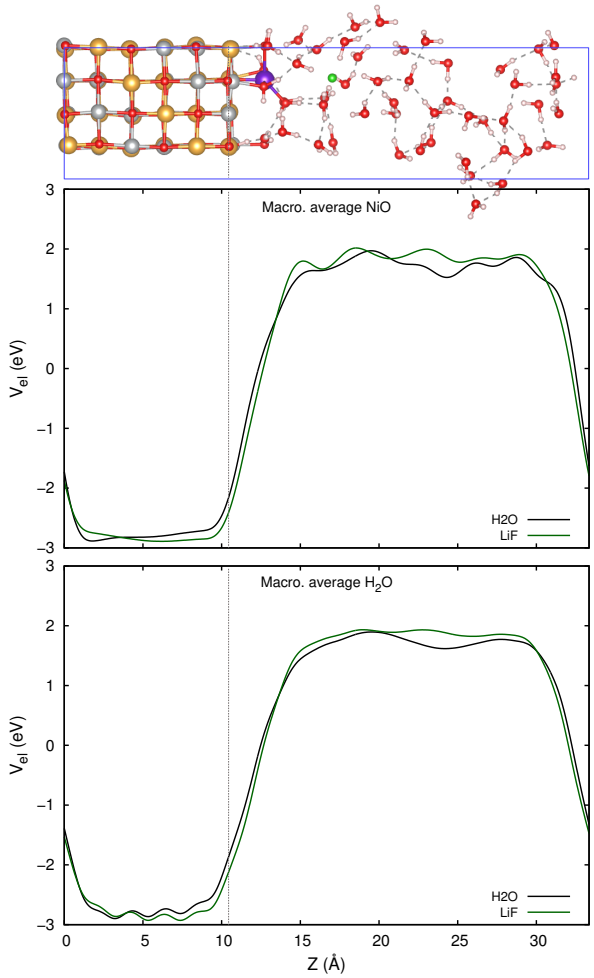

Figure 4: (Top panel) Structure of the NiO/water interface in the presence of Li^+ and F^- ions, extracted from the AIMD simulations (top panel); (Middle panel) Time average of the macroscopic averaged electrostatic potential across the interface in pure water (H_2O) and in the presence of Li^+/F^- ions (LiF) computed using the average distance between NiO layers; (Bottom panel) Same quantities reported in the middle panel, but with the macroscopic average performed using the distance between water's oxygen atoms obtained from the first peak of the O-O radial pair distribution function.

3.3 Structure and dynamics of the C343@NiO interfaces models

To study how cations in the electrolyte affect the structure of the C343@NiO interface, we compare AIMD trajectories in pure water with those in the presence of Li^+/F^-. In Figure 5 we plot the time evolution of the dye's bidentate anchoring to the surface by monitoring the two Ni-O bond lengths. The bonds are marked in green and blue in panel (a) of Figure 5, while in panels (b-d) we show the results obtained for the three interface systems considered here.

In the case of C343@NiO in pure water (5b), the dye remains anchored throughout the AIMD trajectory, even though the two Ni-O bonds are not equivalent and we observe a dynamic equilibrium between monodentate and bidentate bindings.[46] The bond labeled in green fluctuates slightly less and shows a smaller mean value compared to the one in blue. The averaged bond lengths are 2.11±0.09 Å and 2.22±0.13 Å for the green and the blue bond, respectively. The reason behind this difference is presumably the chemisorption of

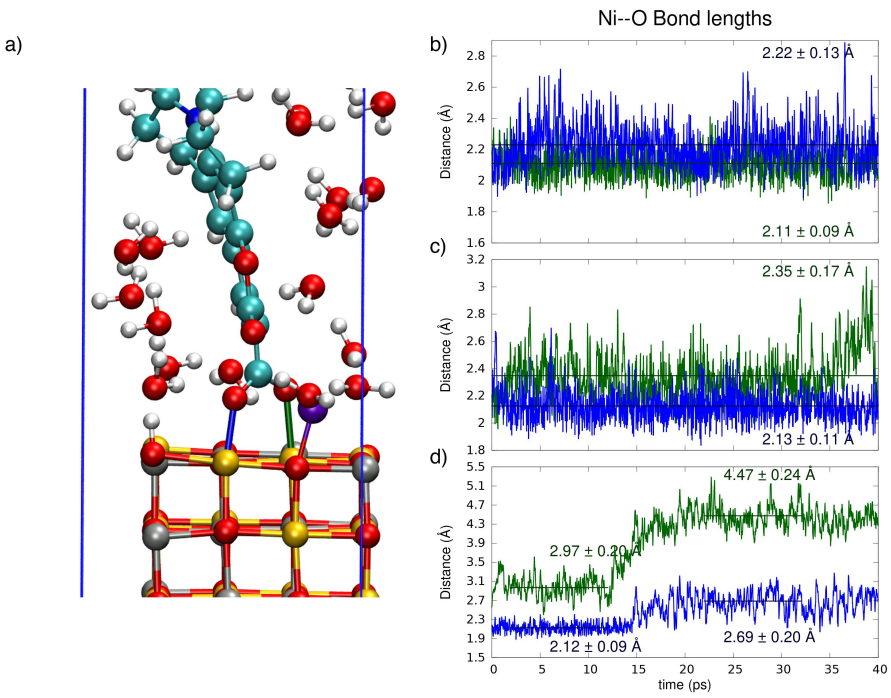

Figure 5: Ni-O(C343) bond distances computed along the 43 ps trajectories for the system in pure water (b), for the systems in the presence of LiF with the F^- close (c) and far (d) from the NiO surface. The green and blue curves in panels (b-d) correspond to the green and blue bonds shown in panel (a).

water molecules at the NiO surfaces, interacting with the dye's carboxylic group and weakening the bonds with the substrate.[46]

When Li^+ adsorbs at a surface, it constrains the movements of neighboring water molecules, attracted by its positive charge. As shown by the comparison between panel 5c and panel 5d, the strength of the O-Ni bonds changes significantly when Li^+/F^- ions are included in the solvent, depending on the anion's position. In the NiO@[Li^+ C343 F^-] case (panel c) the system's dynamics closely resemble those observed in pure water (panel b). When F^- is confined above the dye, Figure 5d, the bidentate anchoring becomes unstable from the outset. The C343 molecule remains weakly bound in a bidentate manner between 2 and 12 ps, with the green-marked bond becoming highly elongated and fluctuating significantly around an average value of 2.97±0.2 Å. In contrast, the blue-marked Ni-O bond length remains consistent with values observed for the C343@NiO interface in pure water, averaging 2.12±0.09 Å. After approximately 13 ps the anchoring switches to a monodentate mode, indicating the tendency for the dye to undergo definitive desorption. During the 22–32 ps interval, the Ni-O bond lengths increase to 2.69±0.2 Å (blue bond) and 4.47±0.24 Å (gren bond), respectively. This behavior can be explained by examining the distances between Li^+ and the two oxygen atoms of the carboxylic group, as shown in Figure S6 in the Supporting Information. During the 2–12 ps interval, where unstable bidentate binding is observed, both carboxylic oxygen atoms are attracted to Li^+, with distances of 2.10 Å ± 0.17 (green) and 2.65 Å ± (blue). Comparing Figure 5 with Figure S6, reveals that the oxygen atom moving further from the substrate (green) interacts most strongly with the cation. Moreover, the transition from weak bidentate binding to pure monodentate is accompanied by the

stabilization of the Li-O bond involving the oxygen atom still bound to the substrate (blue).This, in turn, weakens the Li-O bond with the oxygen atom that moves away from the substrate (green).

In the NiO@[Li^+ C343 F^-] system, LiF affects the stability of dye-surface anchoring differently. The computed Ni-O bond lengths displayed in Figure 5c) do not indicate any tendency to desorption, but a preference for monodentate binding, similar to the C343@NiO interface in pure water. During the last 5 ps, indeed, the green bond elongates significantly, confirming a switch to monodentate binding. Inspection of the distances between the oxygen atoms of the carboxylic group and the Li^+ ion (Figure S6) provides valuable insights into this different behavior. Unlike in the NiO@[Li^+ C343]F^- system, the cation quickly ($\sim$ 1 ps) moves to a free neighboring Ni atom to approach a favorably oriented water molecule and complete its solvation shell. The freedom of the Li^+ ion is primarily due to the lack of interaction with the dye-COO^- group, as the presence of fluorine significantly restricts the movement of C343, preventing the reorientation needed to facilitate this interaction. The root-mean-square deviation (RMSD) of the C343 (Figure S5) confirms that the dye experiences only modest fluctuations. As a matter of fact, the RMSD is always lower than the one computed for the dye in pure water, while, as expected, the highest RMSD was found for the NiO@[Li^+ C343]F^- system.

To summarize, as experimentally observed, we demonstrate that the Li^+ ion negatively affects the stability of the dye on the substrate, with the weakening of the dye-substrate bonds in the presence of the electrolyte representing the initial step toward dye desorption. While our results primarily emphasize the role of Li^+ in modulating the dye's anchoring, based on the observed explicit interaction between the dye and the cation, we also acknowledge that F^- may play a role in influencing dye stability. This effect may be considered partly an artifact of our computational setup, as, when F^- is closer to the interface, in the employed simulation box, the dye experiences restraint movements that limit its interaction with Li^+ adsorbed on the surface. This constraint may bias the dye desorption process in our model compared to what is typically experimentally observed

3.4 Electronic structure and charge separation properties of the C343@NiO interface models

3.4.1 Driving force for hole injection

As already stated, electrolyte additives, such as lithium or magnesium salts are widely used in DSSCs to modulate the photocurrent, J_{SC}, and the open-circuit voltage, V_{oc}. To assess whether the presence of lithium salts in the electrolytic solution has a significant effects on the electronic structure of the C343-sensitized NiO interface we calculated, along the MD trajectories of the three model systems, the driving force for the hole transfer, which is defined as the energy difference between the VBM of the NiO slab and the dye's HOMO. Additionally, we analyzed the alignment of the energy levels with respect to the potential of the bulk water (section 3.4.2), and the electronic coupling between the dye levels and the NiO VB states (section 3.4.3).

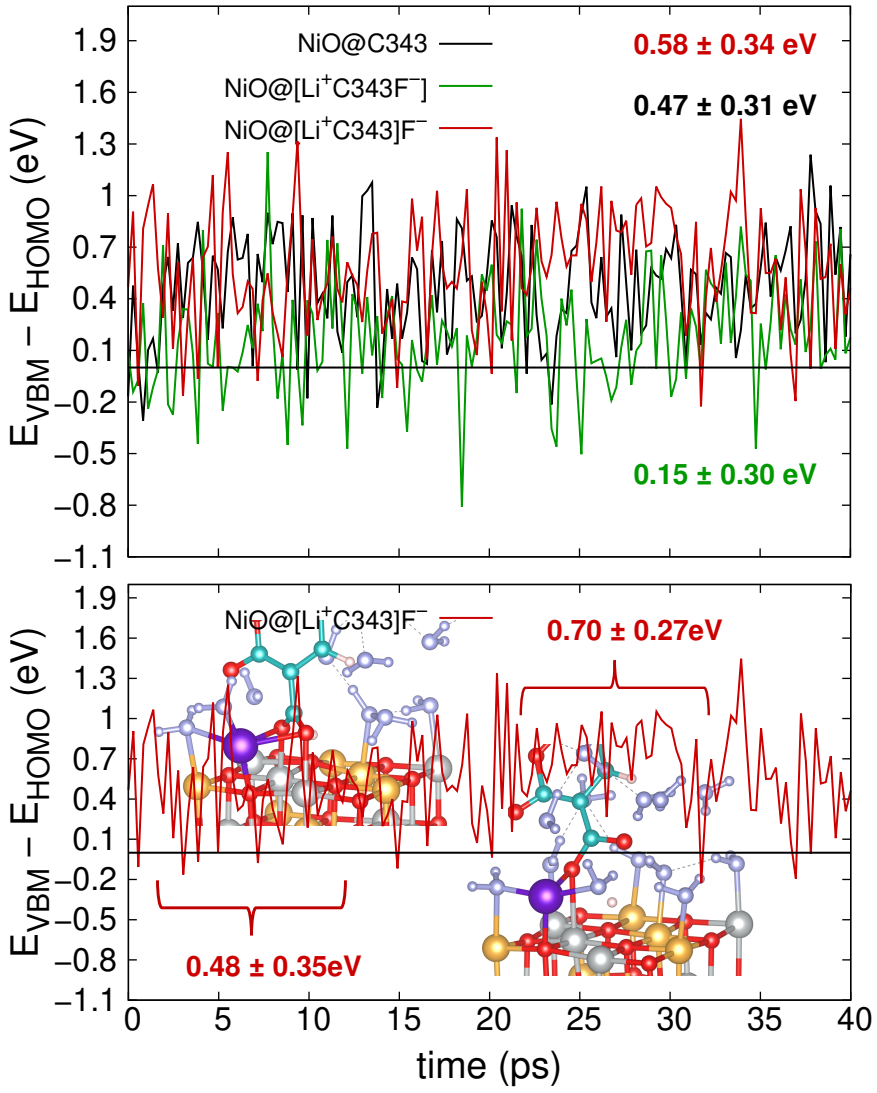

Figure 6: Calculated difference between the VBM of NiO and HOMO of C343 for $\sim$ 150 snapshots extracted from the MD production runs for the three interface systems considered in this work and displayed in Figure 1.

The top panel of Figure 6 displays the time evolution of the calculated driving force for the three interface systems. As evident, the mean values of the averaged driving forces in pure water (black line) and the NiO@[Li^+ C343]F^- system (red line) are quite similar, differing by 0.1 eV, with comparable standard deviations. Specifically, the mean values along with their standard deviations are 0.47 $\pm$ 0.31 eV and 0.58 $\pm$ 0.34 eV for pure water and the NiO@[Li^+ C343]F^- system, respectively. Thus, our calculations do not predict the expected lowering in the driving force and seems, even, to indicate its slight increase. In both cases, the positive sign implies that the hole transfer from the dye to NiO is energetically feasible. Conversely, the calculated driving force in the NiO@[Li^+ C343 F^-] system shows a significantly lower mean value of 0.15 $\pm$ 0.30 eV. In addition, it often exhibits negative E_{VBM} - E_{HOMO} differences, indicating an unfavorable alignment for hole transfer in numerous configurations (26% compared to 9% in the NiO@C343 and NiO@[Li^+

C343]F^- systems). Careful analysis reveals that huge effect on the energy levels alignments and decrease in the driving force cannot be attributed to charge transfer phenomena from LiF to the NiO@C343 interface, as this transfer is negligible in all systems. This is evident from the fact that the charge associated with the NiO slab remains close to zero regardless of the presence of Li^+/F^- ions, indicating minimal transfer even when Li^+ adsorbed (Figures S7-S9). Instead, the decrease can be attributed to the destabilization of the HOMO, which is delocalized over the dye skeleton, caused by the proximity of the F^- ion. However, it is important to point out that the HOMO destabilization may be overestimated in our calculations due to the small size of our simulation cell, limiting the mutual mobility of the anion and the dye.

To further investigate the unexpected slight increasing in the calculated average driving force for the NiO@[Li^+ C343]F^- system, we calculated the driving forces for the two time intervals of the AIMD analyzed in Section 3.3, namely 2-12 ps (bidentate anchoring) and 22-32 ps (monodentate anchoring). It has been, indeed, found that the change in the anchoring geometry induces changes in the relative energy levels alignment,[44,45] These values are gathered in Table C in the Supporting Information for all three systems. As is apparent the NiO@[Li^+ C343]F^- system shows significantly different driving forces in the two analyzed time intervals. When the dye is anchored in a weak bidentate binding mode (2-12 ps) the driving force is equivalent to that obtained without LiF and about 0.22 eV lower compared to that calculated upon switching to the monodentate anchoring (22-32 ps), in line with the findings of previous theoretical calculations.[44] This behavior can be traced back to the variation of the interfacial dipole concomitant to the breaking of one of the O-Ni anchoring bonds, similarly to what found by some of us for the phosphonate anchoring group.[45]

3.4.2 Alignment of the band edges relative to the water bulk potential

By analyzing the driving force values calculated along the MD trajectories, we are, however, unable to distinguish the pure electrostatic effects caused by the presence of the Li^+ and F^- ions from the electronic effects arising from the mixing of the dye's and NiO's states. To assess the interfacial electrostatic and obtain the potential drop at the NiO/C343 interface, we computed the evolution of the electrostatic potential along the MD trajectories, as previously done for dye-free interfaces. In Figure 7 we show the time-averaged electrostatic potential (V_{el}) for the three C343@NiO model systems. As is apparent, the presence of Li^+/F^- generates an electric field that is well screened in the bulk water region but that gives rise to a very large slope of the potential inside NiO. Since we are interested in the interfacial charge transfer, we concentrate only on the potential drop across the NiO/dye interface (ΔV^{interf}). This quantity is the difference between the potential close to the NiO surface, measured between the first and second NiO layer, and the potential in the bulk electrolyte. To be consistent with what has been done for the NiO slab in water, we average the bulk water potential in a 4 Å window centered in the middle of the bulk water region. Table 2 collects the values of the electrostatic potential (ΔV^{interf}) in NiO and dye regions, aligned with respect to the bulk water potential.

In the case of the NiO@C343 system, the difference amounts to approximately 0.73 eV. The presence of LiF in the simulation increases ΔV^{interf}, with the increase becoming more significant as the distance

between the NiO@C343 interface and the fluorine anion increases. For NiO@[Li^+ C343F^-], the ΔV^{interf} difference is 0.09 eV larger than for the neutral system, whereas for the NiO@[Li^+ C343]F^- system, the difference is 0.17 eV larger. Thus, the correlation between the averaged driving force and the ΔV^{interf} exists solely for the NiO@C343 and NiO@[Li^+ C343]F^- systems, since NiO@[Li^+ C343F^-], which shows an intermediate ΔV^{interf}, yields in turn to the smallest average driving force. The absence of a clear E_{VBM} - $E_{HOMO}/\Delta V^{interf}$ correlation for this system brings us to leads us to conclude that the decrease in the driving force cannot be attributed solely to a shift in the electrostatic potential across the interface. Instead, it is more likely a result of a partial charge transfer from the F^- ion to the dye, which destabilizes its occupied molecular orbitals, as discussed above.

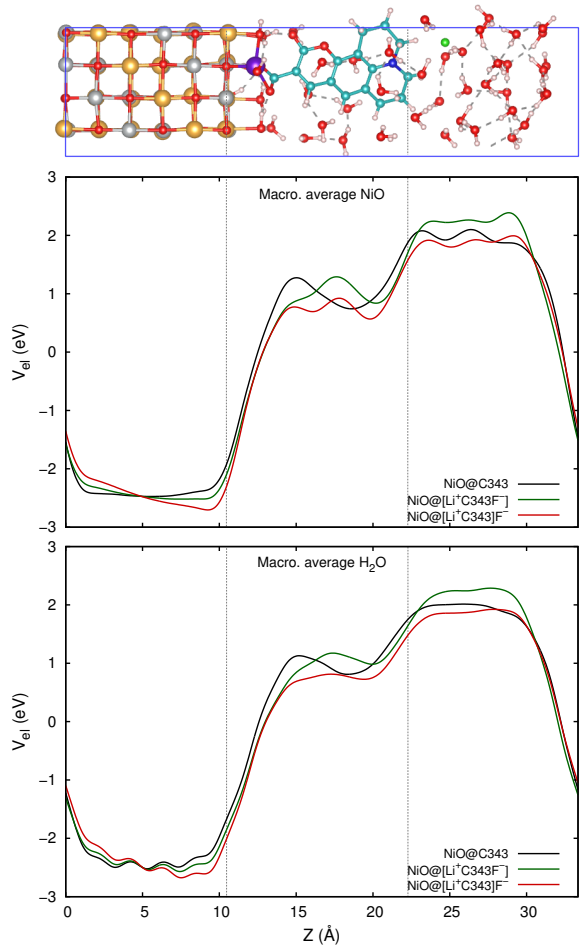

Figure 7: C343@NiO interface in aqueous solution extracted from the MD simulations of system iii) (top panel); time averaged of the macroscopic averaged electrostatic potential across the interface for the three model systems calculated by using the distance between NiO planes (middle panel) and the O-O distance in bulk water (bottom panel).

Table 2: V_{el} (eV) for the NiO and the C343 and the difference between the dye and NiO potentials ($\Delta V^{interf.}$) computed along MD simulations of the three systems displayed in Figure 1 and referred to the bulk water potential.

	NiO@C343	NiO@[Li^+ C343F^-]	NiO@[Li^+ C343]F^-
NiO	-4.28	-4.71	-4.42
C343	-3.55	-3.89	-3.52
$\Delta V^{interf.}$	0.73	0.82	0.90

3.4.3 Electronic coupling and hole injection rates

On overall, the computed lifetime broadening values reported in Table 3 depict a rather modest coupling between the dye and the substrate. The mean value of the lifetime broadening shows minimal variations along dynamics for C343@NiO in pure water, with $\hbar\Gamma$ values of the order of 30 meV and an estimated hole-transfer time of about 30 fs. Note that these values are comparable to those computed in dye@TiO_2 models for dyes bearing non-conjugated anchoring groups, where the LUMOs are poorly coupled with the CB states of the substrate.[65,69] In contrast, strongly coupled systems are characterized by $\hbar\Gamma$ of 200-300 meV and calculated injection rates of 3-2 fs.[69] Although the calculated electron transfer rates do not quantitatively match the measured values, the predicted one-order-of-magnitude increase when passing from strongly to weakly coupled systems aligns with experimental observations. These experiments report ultrafast injection times < 100 fs for conjugated dye@TiO_2 systems and longer rates of about 200-300 fs for C343 sensitized NiO interfaces.[21,68]

Moving to the systems with LiF, we quantified the effect of the change in the anchorage on the electronic coupling and on the hole transfer time (τ), by separately calculating $\hbar\Gamma$ into the two considered time intervals. Although LiF significantly impacts the energy level alignment, it only slightly influences the electronic coupling, which is nevertheless globally larger compared to the one computed for the interface in pure water. For NiO@[Li^+C343]F^- system, as expected, the transition from bidentate to monodentate anchoring reduces $\hbar\Gamma$, by half, from approximately 40 meV to 20 meV.[70] These calculations show us that the increase of the driving force induced by the presence of LiF is not accompanied by a corresponding increase in electronic coupling, despite the higher density of isoenergetic NiO states available to hybridize with the HOMO compared to the interface in pure water.

Table 3: Calculated lifetime broadening ($\hbar\Gamma$) and hole-transfer time (τ) along the MD simulations of the three C343@NiO interfaces modeled in this work using the dye embedded in implicit water as a reference. For the systems including LiF, the ions have also been considered in the reference.

	NiO@C343	NiO@[Li^+C343]F^-	NiO@[Li^+C343F^-]
	Time interval: $\mathbf{2-12}$ **ps**		
$\hbar\Gamma$ (meV)	29.19± 14.11	38.98 ± 22.11	50.48 ± 15.87
τ (fs)	28.07±9.96	23.83 ± 13.66	14.98 ± 5.09
	Time interval: $\mathbf{22-32}$ **ps**		
$\hbar\Gamma$ (meV)	27.58 ± 9.48	20.31± 15.77	39.56 ± 19.23
τ (fs)	28.82±11.45	69.79 ± 64.83	21.20 ± 9.73

By correlating the electronic coupling in Table 3 and the driving forces in Figure 6 and Table C, we

conclude that the calculated increase in driving force does not directly result from the lithium cation's effect on the relative alignment of energy levels across the NiO/C343 interface. Instead, it arises because the presence of lithium favors a change in the dye's anchoring mode, which in turn alters its electrostatic potential. However, this bidentate-to-monodentate transition is however the initial step toward the eventual desorption of the dye, as experimentally demonstrated.

Interestingly, the $\hbar\Gamma$ values predicted for NiO@[Li^+C343F^-] system are the highest listed in Table 3, ranging from 40 to 50 meV This is the direct consequence of the nearly null driving force calculated for this system. The near-degeneracy between the HOMO level and the NiO VBM (Table C in Supporting Information) enables significant coupling between the HOMO and the spatially proximate surface states, that dominate the valence band edge of the semiconductor. [46]

4 Conclusions

In this study we report a detailed atomistic investigation, supported by electrochemical measurements, of the role played by Li^+ ions in dye-sensitized NiO interfaces, disentangling and quantifying both their direct and indirect effects on dye anchoring, relative energy level alignment and hole-transfer kinetics.

Electrochemical characterization shows that the the presence of Li^+ ions results in a 100 mV positive shift of NiO potential. Compared to larger cations such as TBA^+, Li^+ ions have a higher charge density and adsorb more strongly onto the NiO surface, making them critical in determining the potential of NiO. We found that NiO in an aqueous solution shows Nernstian behavior with a slope of ca. 60 mV/pH for the Ni(II)/(III) process (wave I). Wave II is also controlled by pH but with a slope further from ideality due to wave broadening at certain pHs. The theoretical band alignment revealed that the presence of Li^+ in the simulation box causes a significant downshift (ca. 0.18 eV) of VBM, which is near-quantitative agreement with experimental values. Experimental and theoretical investigations suggest that the presence of Li^+ weakens the bond between C343 and NiO, leading to faster and more extensive dye desorption from the NiO surface. However, the simulation results are highly sensitive to the interface structure, which is also crucial for the efficiency of interfacial hole transfer. When the fluorine anion is located within the dye layer, as in the NiO@[Li^+C343F^-] system, the driving force decreases with respect to the simulation without LiF. In contrast, in the NiO@[Li^+C343]F^- system, the driving force shows a slight decrease when the coumarin forms a partially bidentate bond with the substrate, and a slight increase when one of the two bonds is eventually broken. These differences cannot be attributed solely to electrostatic effects, as the difference between the electrostatic potential of the dye and that of the NiO is similar in the three systems. Instead, the coupling between NiO and the dye is strongly influenced by the dynamic structure of the C343@NiO interfaces, with the different driving forces resulting from coupling with states in distinct regions of the density of states.

Our results demonstrate that accurately predicting the energetics and hole transfer kinetics at realistic dye/NiO/solvent interfaces is highly challenging. This requires the simultaneous consideration of multiple

factors, such as thermal fluctuations, electrolyte effects, and solvation, while employing an adequate level of theory. The complexity of the structural models we developed—incorporating the dye, semiconductor slab, explicit water, and potential-determining ions—along with the methodologies used, such as AIMD simulations, GW calculations, and the determination of electronic coupling and hole transfer rates, clearly surpasses the current state-of-the-art for NiO-dye sensitized interfaces. These advancements provide valuable physical insights and computational progress that may be leveraged to further enhance the efficiency of p-type DSSCs.

Supporting Information

Cyclic voltammetry: electrochemical behavior under varying conditions. Molecular dynamics: structural and energetic insights of NiO interfaces. Bader charge analysis and free energy profiles for lithium adsorption.

Acknowledgements

M. P. and A. S. acknowledge HPC resources from mesocentre EXPLOR of the University of Lorraine (project 2018CPMXX0602). S.P. acknowledges financial support from ICSC – Centro Nazionale di Ricerca in High Performance Computing, Big Data and Quantum Computing, and from NEST - Network 4 Energy Sustainable Transition (PE00000021), both funded by European Union – NextGenerationEU.

References

(1) Meethal, S. M.; Pradhan, S. C.; Velore, J.; Varughese, S.; Pillai, R. S.; Sauvage, F.; Hagfeldt, A.; Soman, S. Asymmetric dual species copper(ii/i) electrolyte dye-sensitized solar cells with 35.6% efficiency under indoor light. *J. Mater. Chem. A* **2024**, *12*, 1081–1093.

(2) Kokkonen, M.; Talebi, P.; Zhou, J.; Asgari, S.; Soomro, S. A.; Elsehrawy, F.; Halme, J.; Ahmad, S.; Hagfeldt, A.; Hashmi, S. G. Advanced research trends in dye-sensitized solar cells. *J. Mater. Chem. A* **2021**, *9*, 10527–10545.

(3) Pastore, M.; Caramori, S.; Gros, P. C. Iron-Sensitized Solar Cells (FeSSCs). *Acc. Chem. Res.* **2024**, *57*, 439–449.

(4) Muñoz García, A. B. et al. Dye-sensitized solar cells strike back. *Chem. Soc. Rev.* **2021**, *50*, 12450–12550.

(5) Fei, L.; Lei, L.; Meyer, T. J.; Wang, D. Dye-Sensitized Photocathodes Assembly and Tandem Photoelectrochemical Cells for CO2 Reduction. *Acc. Mater. Res.* **2024**, *5*, 124–135.

(6) Brennaman, M. K.; Dillon, R. J.; Alibabaei, L.; Gish, M. K.; Dares, C. J.; Ashford, D. L.; House, R. L.; Meyer, G. J.; Papanikolas, J. M.; Meyer, T. J. Finding the Way to Solar Fuels with Dye-Sensitized Photoelectrosynthesis Cells. *J. Am. Chem. Soc.* **2016**, *138*, 13085–13102.

(7) Zhu, Y.; Wang, D.; Huang, Q.; Du, J.; Sun, L.; Li, F.; Meyer, T. J. Stabilization of a molecular water oxidation catalyst on a dye- sensitized photoanode by a pyridyl anchor. *Nature Commun.* **2020**, *11*, 4610.

(8) Young, K. J.; Martini, L. A.; Milot, R. L.; Snoeberger III, R. C.; Batista, V. S.; Schmuttenmaer, C. A.; Crabtree, R. H.; Brudvig, G. W. Light-driven water oxidation for solar fuels. *Coord. Chem. Rev.* **2012**, *256*, 2503–2520.

(9) Ren, Y.; Zhang, D.; Suo, J.; Cao, Y.; Eickemeyer, F. T.; Vlachopoulos, N.; Zakeeruddin, S. M.; Hagfeldt, A.; Grätzel, M. Hydroxamic acid pre-adsorption raises the efficiency of cosensitized solar cells. *Nature* **2023**, *613*, 60–65.

(10) Nikolaou, V.; Charisiadis, A.; Charalambidis, G.; Coutsolelos, A. G.; Odobel, F. Recent advances and insights in dye-sensitized NiO photocathodes for photovoltaic devices. *J. Mater. Chem. A* **2017**, *5*, 21077–21113.

(11) Benazzi, E.; Mallows, J.; Summers, G. H.; Black, F. A.; Gibson, E. A. Developing photocathode materials for p-type dye-sensitized solar cells. *J. Mater. Chem. C* **2019**, *7*, 10409–10445.

(12) Wrede, S.; Tian, H. Towards sustainable and efficient p-type metal oxide semiconductor materials in dye-sensitised photocathodes for solar energy conversion. *Phys. Chem. Chem. Phys.* **2020**, *22*, 13850–13861.

(13) Dimple, D.; Lebègue, S.; Pastore, M. Dye Anchoring on CuCrO2 Surfaces for p-Type Dye-Sensitized Solar Cell Applications: An Ab Initio Study. *ACS Appl. En. Mater.* **2021**, *4*, 6180–6190.

(14) Zhu, K.; Mul, G.; Huijser, A. Dye-sensitized NiO photocathodes: Research progress, current mechanistic understanding, and research perspectives. *Chem. Phys. Rev.* **2024**, *5*.

(15) Cheng, F.; Pavliuk, O.; Hardt, S.; Hunt, L. A.; Cai, B.; Kubart, T.; Hammarström, L.; Plumeré, N.; Berggren, G.; Tian, H. Embedding biocatalysts in a redox polymer enhances the performance of dye-sensitized photocathodes in bias-free photoelectrochemical water splitting. *Nat. Commun.* **2024**, *15*, 3202.

(16) Giannoudis, E. et al. Hydrogen production at a NiO photocathode based on a ruthenium dye–cobalt diimine dioxime catalyst assembly: insights from advanced spectroscopy and post-operando characterization. *ACS Appl. Mater. Interfaces* **2021**, *13*, 49802–49815.

(17) D'Amario, L.; Boschloo, G.; Hagfeldt, A.; Hammarström, L. Tuning of Conductivity and Density of States of NiO Mesoporous Films Used in p-Type DSSCs. *J. Phys. Chem. C* **2014**, *118*, 19556–19564.

(18) Odobel, F.; Pellegrin, Y.; Gibson, E.; Hagfeldt, A.; Smeigh, A.; Hammarström, L. Recent advances and future directions to optimize the performances of p-type dye-sensitized solar cells. *Coordination Chemistry Reviews* **2012**, *256*, 2414–2423.

(19) Zhang, L.; Favereau, L.; Farré, Y.; Mijangos, E.; Pellegrin, Y.; Blart, E.; Odobel, F.; Hammarström, L. Ultrafast and slow charge recombination dynamics of diketopyrrolopyrrole NiO dye sensitized solar cells. *Phys. Chem. Chem. Phys.* **2016**, *18*, 18515–18527.

(20) Antila, L. J.; Ghamgosar, P.; Maji, S.; Tian, H.; Ott, S.; Hammarström, L. Dynamics and Photochemical H2 Evolution of Dye@NiO Photocathodes with a Biomimetic FeFe-Catalyst. *ACS Energy Lett.* **2016**, *1*, 1106–1111.

(21) Brown, A. M.; Antila, L. J.; Mirmohades, M.; Pullen, S.; Ott, S.; Hammarström, L. Ultrafast Electron Transfer Between Dye and Catalyst on a Mesoporous NiO Surface. *J. Am. Chem. Soc.* **2016**, *138*, 8060–8063.

(22) Smeigh, A. L.; Pleux, L. L.; Fortage, J.; Pellegrin, Y.; Blart, E.; Odobel, F.; Hammarström, L. Ultrafast recombination for NiO sensitized with a series of perylene imide sensitizers exhibiting Marcus normal behaviour. *Chem. Commun.* **2012**, *48*, 678–680.

(23) Chia-Ching, W.; Cheng-Fu, Y. Investigation of the properties of nanostructured Li-doped NiO films using the modified spray pyrolysis method. *Nanoscale Res. Lett.* **2013**, *8*, 33.

(24) Flynn, C. J. et al. Site-selective passivation of defects in NiO solar photocathodes by targeted atomic deposition. *ACS Appl. Mater. Interfaces* **2016**, *8*, 4754–4761.

(25) Zhu, K.; Frehan, S. K.; Jaros, A. M.; ONeill, D. B.; Korterik, J. P.; Wenderich, K.; Mul, G.; Huijser, A. Unraveling the Mechanisms of Beneficial Cu-Doping of NiO-Based Photocathodes. *J. Phys. Chem. C* **2021**, *125*, 16049–16058.

(26) Xu, X.; Li, L.; Huang, J.; Jin, H.; Fang, X.; Liu, W.; Zhang, N.; Wang, H.; Wang, X. Engineering Ni3+ Cations in NiO Lattice at the Atomic Level by Li+ Doping: The Roles of Ni3+ and Oxygen Species for CO Oxidation. *ACS Catal.* **2018**, *8*, 8033–8045.

(27) Xiao, Z.; Zhou, W.; Zhang, N.; Liao, C.; Huang, S.; Chen, G.; Chen, G.; Liu, M.; Liu, X.; Ma, R. Lithium doped nickel oxide nanocrystals with a tuned electronic structure for oxygen evolution reaction. *Chem. Commun.* **2021**, *57*, 6070–6073.

(28) McCullough, S. M.; Evans, J. M.; Moot, T.; Taggart, A. D.; Troian-Gautier, L.; Cahoon, J. F. Cation Effects in p-Type Dye-Sensitized Solar Cells. *ACS Appl. Energy Mater.* **2020**, *3*, 1496–1505.

(29) Liu, H.; Xiang, W.; Tao, H. Probing the influence of lithium cation as electrolyte additive for the improved performance of p-type aqueous dye sensitized solar cells. *J. Photochem. Photobiol. A* **2017**, *344*, 199–205.

(30) Liu, Y.; Hagfeldt, A.; Xiao, X.-R.; Lindquist, S.-E. Investigation of influence of redox species on the interfacial energetics of a dye-sensitized nanoporous TiO2 solar cell. *Sol. Energy Mater Sol. Cells* **1998**, *55*, 267–281.

(31) Agrawal, S.; Leijtens, T.; Ronca, E.; Pastore, M.; Snaith, H.; De Angelis, F. Modeling the effect of ionic additives on the optical and electronic properties of a dye-sensitized TiO2 heterointerface: absorption, charge injection and aggregation. *J. Mater. Chem. A* **2013**, *1*, 14675–14685.

(32) Reddy-Marri, A.; Marchini, E.; Cabanes, V. D.; Argazzi, R.; Pastore, M.; Caramori, S.; Gros, P. C. Panchromatic light harvesting and record power conversion efficiency for carboxylic/cyanoacrylic Fe(ii) NHC co-sensitized FeSSCs. *Chem. Sci.* **2023**, *14*, 4288–4301.

(33) Reddy Marri, A.; Marchini, E.; Cabanes, V. D.; Argazzi, R.; Pastore, M.; Caramori, S.; Gros, P. C. Record power conversion efficiencies for iron(ii)-NHC-sensitized DSSCs from rational molecular engineering and electrolyte optimization. *J. Mater. Chem. A* **2021**, *9*, 3540–3554.

(34) D'Amario, L.; Föhlinger, J.; Boschloo, G.; Hammarström, L. Unveiling hole trapping and surface dynamics of NiO nanoparticles. *Chem. Sci.* **2018**, *9*, 223–230.

(35) Pastore, M.; Selloni, A.; Fantacci, S.; De Angelis, F. In *First Principles Approaches to Spectroscopic Properties of Complex Materials*; Di Valentin, C., Botti, S., Cococcioni, M., Eds.; Springer Berlin Heidelberg: Berlin, Heidelberg, 2014; pp 1–45.

(36) Jakubikova, E.; Bowman, D. N. Fe(II)-Polypyridines as Chromophores in Dye-Sensitized Solar Cells: A Computational Perspective. *Acc. Chem. Res.* **2015**, *48*, 1441–1449.

(37) Akimov, A. V.; Neukirch, A. J.; Prezhdo, O. V. Theoretical Insights into Photoinduced Charge Transfer and Catalysis at Oxide Interfaces. *Chem. Rev.* **2013**, *113*, 4496–4565.

(38) Yang, Z.; Li, K.; Lin, C.; Devereux, L. R.; Zhang, W.; Shao, C.; Cole, J. M.; Cao, D. Predicting Device Parameters for Dye-Sensitized Solar Cells from Electronic Structure Calculations to Reproduce Experiment. *ACS Appl. Energy Mater.* **2020**, *3*, 4367–4376.

(39) Zhang, X.; Shen, J.-X.; Van de Walle, C. G. First-Principles Simulation of Carrier Recombination Mechanisms in Halide Perovskites. *Adv. Energy Mater.* **2020**, *10*, 1902830.

(40) Zhou, X.; Jankowska, J.; Dong, H.; Prezhdo, O. V. Recent theoretical progress in the development of perovskite photovoltaic materials. *J. Energy Chem.* **2018**, *27*, 637–649.

(41) Li, W.; She, Y.; Vasenko, A. S.; Prezhdo, O. V. Ab initio nonadiabatic molecular dynamics of charge carriers in metal halide perovskites. *Nanoscale* **2021**, *13*, 10239–10265.

(42) Xu, M.; Zhang, M.; Pastore, M.; Li, R.; De Angelis, F.; Wang, P. Joint electrical, photophysical and computational studies on D-π-A dye sensitized solar cells: the impacts of dithiophene rigidification. *Chem. Sci.* **2012**, *3*, 976–983.

(43) Pantaler, M. et al. Revealing Weak Dimensional Confinement Effects in Excitonic Silver/Bismuth Double Perovskites. *JACS Au* **2022**, *2*, 136–149.

(44) Muñoz García, A. B.; Pavone, M. Structure and energy level alignment at the dye-electrode interface in p-type DSSCs: new hints on the role of anchoring modes from ab initio calculations. *Phys. Chem. Chem. Phys.* **2015**, *17*, 12238–12246.

(45) Piccinin, S.; Rocca, D.; Pastore, M. Role of Solvent in the Energy Level Alignment of Dye-Sensitized NiO Interfaces. *J. Phys. Chem. C* **2017**, *121*, 22286–22294.

(46) Segalina, A.; Lebègue, S.; Rocca, D.; Piccinin, S.; Pastore, M. Structure and Energetics of Dye-Sensitized NiO Interfaces in Water from Ab Initio MD and Large-Scale GW Calculations. *J. Chem. Theory Comput.* **2021**, *17*, 5225–5238.

(47) Kontkanen, O.; Niskanen, M.; Hukka, T.; Rantala, T. Electronic structure of p-type perylene monoimide-based donor–acceptor dyes on the nickel oxide (100) surface: a DFT approach. *Phys. Chem. Chem. Phys.* **2016**, *18*, 14382–14389.

(48) Ma, S.; Liu, W.; Köhn, A. Adsorption geometries and electronic properties of a dipolar phosphonate-based monolayer on the NiO surface. *J. Phys. Chem. C* **2022**, *126*, 5793–5804.

(49) Kontkanen, O. V.; Hukka, T. I.; Rantala, T. T. Electronic structures of three anchors of triphenylamine on a p-type nickel oxide (100) surface: density functional theory with periodic models. *Phys. Chem. Chem. Phys.* **2024**, *26*, 17588–17598.

(50) Zhu, H.; Hagfeldt, A.; Boschloo, G. Photoelectrochemistry of Mesoporous NiO Electrodes in Iodide/Triiodide Electrolytes. *J. Phys. Chem. C* **2007**, *111*, 17455–17458.

(51) Wood, C. J. et al. A comprehensive comparison of dye-sensitized NiO photocathodes for solar energy conversion. *Physical Chemistry Chemical Physics* **2016**, *18*, 10727–10738.

(52) Boschloo, G.; Fitzmaurice, D. Electron Accumulation in Nanostructured TiO_2 (Anatase) Electrodes. *J. Phys. Chem. B* **1999**, *103*, 7860–7868.

(53) Carter, E.; Ciccotti, G.; Hynes, J. T.; Kapral, R. Constrained reaction coordinate dynamics for the simulation of rare events. *Chemical Physics Letters* **1989**, *156*, 472–477.

(54) Sprik, M.; Ciccotti, G. Free energy from constrained molecular dynamics. *The Journal of Chemical Physics* **1998**, *109*, 7737–7744.

(55) Hutter, J.; Iannuzzi, M.; Schiffmann, F.; VandeVondele, J. cp2k: atomistic simulations of condensed matter systems. *Wiley Interdiscip. Rev. Comput. Mol. Sci.* **2014**, *4*, 15–25.

(56) Bussi, G.; Donadio, D.; Parrinello, M. Canonical sampling through velocity rescaling. *J. Chem. Phys.* **2007**, *126*, 014101.

(57) Kresse, G.; Furthmüller, J. Efficient iterative schemes for ab initio total-energy calculations using a plane-wave basis set. *Phys. Rev. B* **1996**, *54*, 11169–11186.

(58) Kresse, G.; Furthmüller, J. Efficiency of ab-initio total energy calculations for metals and semiconductors using a plane-wave basis set. *Comput. Mater. Sci.* **1996**, *6*, 15 – 50.

(59) Kresse, G.; Joubert, D. From ultrasoft pseudopotentials to the projector augmented-wave method. *Phys. Rev. B* **1999**, *59*, 1758–1775.

(60) Cococcioni, M.; de Gironcoli, S. Linear response approach to the calculation of the effective interaction parameters in the LDA + U method. *Phys. Rev. B* **2005**, *71*, 035105.

(61) Mathew, K.; Kolluru, V. S. C.; Mula, S.; Steinmann, S. N.; Hennig, R. G. Implicit self-consistent electrolyte model in plane-wave density-functional theory. *J. Chem. Phys.* **2019**, *151*, 234101.

(62) Ravikumar, A.; Baby, A.; Lin, H.; Brivio, G. P.; Fratesi, G. Femtomagnetism in graphene induced by core level excitation of organic adsorbates. *Sci. Rep.* **2016**, *6*, 24603.

(63) Nelson, R.; Ertural, C.; George, J.; Deringer, V. L.; Hautier, G.; Dronskowski, R. LOBSTER: Local orbital projections, atomic charges, and chemical-bonding analysis from projector-augmented-wave-based density-functional theory. *J. Comput. Chem.* **2020**, *41*, 1931–1940.

(64) Umari, P.; Giacomazzi, L.; De Angelis, F.; Pastore, M.; Baroni, S. Energy-level alignment in organic dye-sensitized TiO2 from GW calculations. *J. Chem. Phys.* **2013**, *139*, 014709.

(65) Persson, P.; Lundqvist, M. J.; Ernstorfer, R.; Goddard, W. A.; Willig, F. Quantum Chemical Calculations of the Influence of Anchor-Cum-Spacer Groups on Femtosecond Electron Transfer Times in Dye-Sensitized Semiconductor Nanocrystals. *J. Chem. Theory Comput.* **2006**, *2*, 441–451.

(66) Marrani, A. G.; Novelli, V.; Sheehan, S.; Dowling, D. P.; Dini, D. Probing the Redox States at the Surface of Electroactive Nanoporous NiO Thin Films. *ACS Appl. Mater. Interfaces* **2013**, *6*, 143–152.

(67) Boschloo, G.; Hagfeldt, A. Spectroelectrochemistry of Nanostructured NiO. *J. Phys. Chem. B* **2001**, *105*, 3039–3044.

(68) Morandeira, A.; Boschloo, G.; Hagfeldt, A.; Hammarström, L. Photoinduced Ultrafast Dynamics of Coumarin 343 Sensitized p-Type-Nanostructured NiO Films. *J. Phys. Chem. B* **2005**, *109*, 19403–19410.

(69) Ronca, E.; Marotta, G.; Pastore, M.; De Angelis, F. Effect of Sensitizer Structure and TiO_2 Protonation on Charge Generation in Dye-Sensitized Solar Cells. *J. Phys. Chem. C* **2014**, *118*, 16927–16940.

(70) Anselmi, C.; Mosconi, E.; Pastore, M.; Ronca, E.; De Angelis, F. Adsorption of organic dyes on TiO2 surfaces in dye-sensitized solar cells: interplay of theory and experiment. *Phys. Chem. Chem. Phys.* **2012**, *14*, 15963–15974.